

1 The piRNA pathway sustains adult neurogenesis by reducing protein synthesis and cellular senescence

2 Authors:

3 Gasperini C.¹, Tuntevski K.¹, Pelizzoli R.¹, Lo Van A.¹, Mangoni D.², Cossu R.M.², Pascarella G.³, Bianchini
4 P.⁴, Bielefeld P.⁵, Scarpato M.², Pons-Espinal M.¹, Sanges R.^{2,6}, Diaspro A.⁴, Fitzsimons C.P.⁵, Carninci P.^{4,7},
5 Gustincich S.² and De Pietri Tonelli D^{1*}

7 Affiliations:

- 8 1) Neurobiology of miRNA Laboratory, Istituto Italiano di Tecnologia, Genoa (Italy)
- 9 2) Central RNA Laboratory, Istituto Italiano di Tecnologia, Genoa, (Italy)
- 10 3) Division of Genomic Technologies, RIKEN Center for Life Science Technologies, Yokohama
11 (Japan)
- 12 4) Nanoscopy, CHT Erzelli, Istituto Italiano di Tecnologia, Genoa (Italy)
- 13 5) Swammerdam Institute for Life Sciences, Faculty of Science, University of Amsterdam (The
14 Netherlands)
- 15 6) Area of Neuroscience, SISSA, Trieste (Italy)
- 16 7) Human Technopole, Milan (Italy).

18 * **Corresponding Author:** Davide De Pietri Tonelli; Istituto Italiano di Tecnologia (IIT); Via Morego 30,
19 16163 Genova (Italy); Phone +39 010 2896 725; E-mail davide.depietri@iit.it

21 Keywords:

22 Adult Neurogenesis; Piwi interacting RNAs; Aging; Translation

24 **Summary**

25 Adult Neural progenitor cells (aNPCs) ensure lifelong neurogenesis in the mammalian hippocampus. Proper
 26 regulation of aNPC fate entails important implications for brain plasticity and healthy aging. Piwi proteins and
 27 the small noncoding RNAs interacting with them (piRNAs) are best known in gonads as repressors of
 28 transposons. Here, we show that Piwil2 (Mili) and piRNAs are abundant in aNPCs of the postnatal mouse
 29 hippocampus and demonstrate that this pathway is essential for proper neurogenesis. Particularly, depleting
 30 the piRNA pathway in aNPCs impaired neurogenesis, increased senescence and accordingly the generation of
 31 reactive glia. Moreover, this manipulation primarily elevated 5S ribosomal RNA, SINEB1 and mRNAs
 32 encoding ribosomal proteins and regulators of translation, resulting in higher polysome density and protein
 33 synthesis upon differentiation. Our results provide evidence of an essential role for the piRNA pathway in
 34 maintaining homeostasis to sustain neural stem cell fate, underpinning its possible involvement in brain
 35 plasticity and successful aging.

36

37 **Introduction**

38 A regulated balance of neural progenitor cells' (aNPCs) quiescence, proliferation and differentiation
39 guarantees lifelong neurogenesis in the adult hippocampus (Altman, 1962; Doetsch et al., 1999), prevents the
40 generation of reactive glia (Encinas et al., 2011; clarke 2018; Sierra et al., 2015), and neurodegeneration
41 (Toda et al., 2019). Understanding the molecular control of aNPCs fate is pivotal to develop novel therapies
42 to prevent or delay age dependent-loss of neurogenesis and related pathological conditions.

43 Piwi belong to an evolutionary conserved subfamily of Argonaute proteins that bind to Piwi-interacting
44 RNAs (piRNAs), single-stranded noncoding RNAs of 21-35 nucleotides. These Piwi proteins and piRNAs
45 (henceforth referred to as the piRNA pathway) are highly abundant in gonads, where they mainly target
46 transposable elements (TEs) for degradation to maintain germline stem cell pools and male fertility (Czech et
47 al., 2018; Ozata et al., 2019).

48 Since its initial discovery, the piRNA pathway has been implicated in regulating gene expression outside of
49 the germline. Moreover, it is preferentially expressed in germ cells, embryonic stem cells and adult stem
50 cells, compared to their differentiated progeny (Rojas-Ríos and Simonelig, 2018). Indeed, expression of Piwi
51 proteins was observed in human hematopoietic stem cells, suggesting a possible role of this pathway in
52 maintaining the stem cell pool (Sharma et al., 2001), whereas its function is dispensable for normal
53 hematopoiesis in mouse (Nolde et al., 2013).

54 In the adult brain, the piRNA pathway was proposed to control synaptic plasticity and memory (Lee et al.,
55 2011; Leighton et al., 2019; Nandi et al., 2016; Zhao et al., 2015). PiRNA levels in neurons, however, are
56 low compared to germline cells (Lee et al., 2011; Nandi et al., 2016), disputing the proposed piRNA pathway
57 function in the nervous system. Apart from gonads, the highest piRNA expression in adult mice has been
58 found in the hippocampus (Perera et al., 2019), however, the specific cell type in which piRNA expression
59 takes place was not identified. Concomitantly, transposable element (TE) expression is high in
60 differentiating NPCs (Muotri et al., 2005), and Piwil1 (Hiwi) was recently shown to regulate human glioma
61 stem cell maintenance (Huang et al., 2021). Thereby, it is reasonable to hypothesize that the piRNA pathway
62 may play a role in aNPCs maintenance and/or differentiation as well.

Here, we demonstrate that the piRNA pathway is enriched in aNPCs, and that its function is essential for proper neurogenesis. Moreover, we show that inhibiting this pathway in aNPCs leads to senescence-associated inflammation in the postnatal mouse hippocampus, a condition which has been linked to age-related impairment of neurogenesis and increase in astroglialogenesis (Clarke et al., 2018; Encinas et al., 2011). Our results implicate the piRNA pathway in the aging of the hippocampal stem cell niche.

Results

Mili expression is abundant in aNPCs and depleted in neurogenesis

As an entry point to investigate Piwi pathway in aNPCs we quantified expression of *Piwi1* (Miwi) *Piwi2* (Mili) and *Piwi4* (Miwi2) mRNAs, which encode the essential proteins for piRNA biogenesis and function in mammals (Czech et al., 2018; Ozata et al., 2019), in cultured aNPCs derived from neural stem cells (NSC) of the adult mouse Dentate Gyrus (DG) (Babu et al., 2011; Pons-Espinal et al., 2017), by RNA sequencing (RNA seq) (Fig.1A). Of the three main Piwi genes in mouse, Mili was the most abundant in aNPCs, and its expression increased transiently upon induction of their spontaneous differentiation. The Mili transcript was particularly more abundant at day 4 (here referred to as days of differentiation DIF 4) upon onset of spontaneous differentiation compared to undifferentiated (i.e., proliferating) aNPCs (DIF 0), whereas it was depleted in differentiated cells (DIF 7-14) (Fig 1A). Similarly, the Mili protein abundance (Fig. 1B) was higher in undifferentiated aNPCs (DIF 0) or early upon onset of vector-induced neurogenesis (DIF 4, neuroblasts) than in differentiated neurons (DIF 7-14). Next, we quantified the abundance of Miwi and Mili proteins in the mouse testis, whole hippocampus, and compared it to the one in undifferentiated aNPCs (Fig. 1C, D). As expected, the Miwi protein was very abundant in testis, but was not detectable in the whole hippocampus or aNPCs (Fig.1C), whereas the Mili protein abundance in aNPCs was about 40% of the one in the testes (Fig. 1D), and about four-fold higher than in primary hippocampal neurons (Fig. 1E). To validate this finding *in vivo*, we used a previously published split-Cre viral approach to selectively label NSCs and their progeny in the hippocampus of postnatal Td-Tomato Cre-reporter mice (Beckervordersandforth et al., 2014; Pons-Espinal et al., 2017). Five days post viral-injection (dpi), we found Mili protein presence in Td-Tomato positive (Td+) NSCs of the subgranular zone (SGZ) of the DG (Fig. 1F). To quantify *Mili* during neurogenesis *in vivo*, we sorted Td+ NSCs and their differentiated progeny at 10 and 30 dpi in the postnatal mouse hippocampus, respectively. The *Mili* transcript was significantly more abundant in Td+ NSCs (10 dpi)

than in adult-born Td+ neurons (30dpi) or Td- cells (Fig. 1G). These results demonstrate that Mili expression is enriched in neural stem/progenitor cells and depleted in their progeny.

Level of piRNAs parallels Mili abundance in neurogenesis

We next wished to determine whether piRNAs are found in aNPCs and quantify their abundance in neurogenesis by small RNA seq (Fig. 2). Following a previously published analysis pipeline (Ghosheh et al., 2016), we identified a total of 725,472 *bona fide* piRNAs, of which 33,396 perfectly aligned (*i.e.*, no mismatch) with those previously annotated in the piRNA database (piRBase (Zhang et al., 2014)), had an average length of 30 nt (Fig. 2A) and bore a 5' uridine (U) bias (Fig. 2B). Moreover, the distance probability between the 5' termini of putative primary and secondary piRNAs was distributed similarly to that of other animals (Gainetdinov et al., 2018), with asymptotic convergence around the '0' mark on the abscissa (Fig. 2C). Mature piRNAs typically bear 2'-O-methylation at their 3' termini, which confers them stability and enables stronger binding to Piwi proteins (Czech et al., 2018; Ozata et al., 2019). We tested whether the putative piRNAs isolated from aNPCs were also methylated by evaluating their resistance to periodate oxidation and alkaline β -elimination, as previously reported (Kirino and Mourelatos, 2007). Indeed, a quantitative real time PCR (qPCR)-based small RNA assay (Taq-Man) indicated that some of the most abundant piRNAs expressed in aNPCs exhibited resistance to periodate treatment, thus indicating their methylation (Fig 2D). In contrast, control synthetic RNAs or endogenous small noncoding RNAs, such as snoRNA bearing a terminal 2',3'-hydroxyl group, were oxidized after the treatment and therefore degraded (Fig 2D). Furthermore, to assess whether putative piRNAs were depending on Mili, we quantified their expression in aNPC cultures upon *Mili* knockdown (Mili-KD) achieved by transducing short-hairpin RNAs targeting *Mili* transcripts, or a scramble short-hairpin RNA as control (or two different synthetic GapmeRs targeting *Mili*, Fig. S1), through a viral vector-mediated protocol *in vitro*. Indeed, reduction of Mili protein abundance in aNPCs (Fig.2E) was sufficient to deplete four of the most highly expressed piRNAs in aNPCs (Fig. 2F and Fig. S1), in agreement with the conclusion that Mili is the most abundant Piwi protein in these cells (Fig.1). Of note, this manipulation did not affect Miwi expression, excluding possible compensatory effects (Fig. S1). Together, this evidence indicates that the most abundant sequences homologous to known piRNAs found in aNPCs fulfill at least five of the criteria that characterize *bona fide* piRNAs (*i.e.*, length, U-Bias, 2'-O-Methylation at the 3' end, inter-distance and MILI dependence).

Genomic mapping of the piRNA reads from aNPCs and their progeny identified 298 clusters perfectly aligning to the mouse genome (Fig 2G and Table S1), with an average size of 168 bases and some of them exceeding 2000 bases, as seen in mouse testes (Aravin et al., 2006; Girard et al., 2006). The piRNA raw reads/cluster averaged around 4700 reads, with two clusters, one located in the chromosome 13 and one in the 17, giving rise to more than 80,000 piRNA reads (Fig. 2G). Analysis of small RNA seq data for directionality suggested a strand bias where the majority of the piRNAs arise unidirectionally, although bidirectional piRNAs were also identified. Analysis of piRNA transcript levels in neurogenesis indicated a transient peak at the onset of differentiation (Fig. 2H DIF 4 and Fig. S1), in agreement with the *Mili* expression pattern. Next, we validated four of the most abundant piRNA clusters in Td+ NSCs sorted from the adult hippocampus confirming their expression *in vivo* (Fig. 2I). Interestingly, one of the piRNA-clusters in our dataset (i.e., piR-cluster 1) is homologous to the human piR-61648 that was recently shown to be selectively expressed in somatic tissues, but is depleted in gonads (Torres et al., 2019) Fig. S1 and Table S1). This observation prompted us to extend our analysis to human NSCs. Analysis of small RNA datasets from the RIKEN FANTOM5 project (De Rie et al., 2017) confirmed the enriched expression of piR-cluster 1, as well as of many additional piRNA clusters in human NSCs compared to differentiated brain cells (Fig. 2L and Table S2). Together, these results indicate that piRNAs are selectively enriched in both mouse and human neural stem/progenitor cells, thus matching the expression of *Mili* (Fig.1).

The piRNA pathway sustains proper neurogenesis

To infer functions of the piRNA pathway in aNPCs differentiation, we knocked down (KD) *Mili* by injecting a synthetic antisense oligonucleotide (GapmeR, MILI KD), or a scrambled GapmeR (Control), in the postnatal mouse hippocampus (Fig. 3A). *Mili*-KD (Fig. 3B) did not alter stemness or growth of aNPCs *in vitro* (Fig. S2) but led to a dramatic increase in the expression of the glial cell marker glial fibrillary acidic protein (GFAP) as early as 48 hours after GapmeR injection *in vivo* (Fig.3B) and *in vitro* (Fig. S2). Inspection of brain sections 30 days after bilateral injections indicated a marked increase in GFAP+ cells with enlarged somas in the ipsilateral hippocampus injected with GapmeR antisense to *Mili*, compared to cells in the contralateral side injected with control GapmeR (Fig. 3C). To ascertain whether GFAP+ cells were actively generated upon *Mili*-KD, we administered bromodeoxyuridine (BrdU) immediately after GapmeRs injection to label dividing cells in a third cohort of mice (Fig. 3A). 30 days after GapmeR

injection, we found that Mili-KD led to a significant increase in adult born GFAP+BrdU+ glial cells at the expense of NeuN+BrdU+ neurons (Fig. 3D). This result was corroborated by gene set analysis in RNA seq data from differentiating aNPCs *in vitro*, showing an enrichment in the expression of astrocyte-related genes and a concomitant deregulation of neuronal fate genes upon piRNA pathway depletion (Fig S2). These results indicated that the piRNA pathway is required to sustain neurogenesis in the postnatal hippocampus at the expense of gliogenesis.

Increased GFAP expression is generally regarded as a hallmark of astrocyte reactivity (Escartin et al., 2021). In agreement, we observed a significant increase in the levels of known reactive glial markers (Clarke et al., 2018; Liddelow et al., 2017) upon Mili KD in the postnatal hippocampus (Fig. 3E). To confirm this result, we took advantage of Kainic Acid injection in the postnatal hippocampus of mice expressing GFP under the control of the NSCs/NPCs specific promoter *Nestin* (Fig. 3F), a treatment previously shown to induce aNSC conversion into reactive glia (Bielefeld et al., 2017; Sierra et al., 2015). Indeed, this treatment reduced levels of the piRNA pathway in sorted *Nestin*-GFP+ NSCs (Fig. 3F). Altogether, these results demonstrate an essential role of the piRNA pathway for proper neurogenesis and suggest that its downregulation mediates reactive gliogenesis in the postnatal mouse hippocampus.

Inhibition of the piRNA pathway in aNPCs results in senescence-associated phenotypes

Conversion of hippocampal NSC into reactive glia, at the expense of neurogenesis, has been observed in normal aging (Clarke et al., 2018), and it has been related to increased neuroinflammation and cellular senescence (Babcock et al., 2021; Martín-Suárez et al., 2019). Whether the piRNA pathway is involved in this mechanism in the brain, is unknown. This prompted us to analyze RNA seq data for senescence-associated secretory phenotype (SASP) in Mili-KD in neuroblasts (Fig. 4A). Interestingly, we found that depletion of the piRNA pathway led to a significant increase in the expression of several immune-modulatory and senescence associated genes in neuroblasts compared to control cells (Fig. 4A). Moreover, after piRNA pathway depletion we observed a higher proportion of cells positive for senescence-associated β -galactosidase (β -gal) as early as 48 hours upon induction of their spontaneous differentiation (Fig. 4B). At the same time point, we immuno-stained aNPCs with anti-KI67 (a protein that is expressed in all phases of the cell cycle except G0 and early G1 (Yu, 1992)) and anti-BrdU antibodies. Quantification of the BrdU + and KI67- cells over total BrdU+ indicated a premature cycle exit upon piRNA pathway depletion (Fig. 4C).

Similarly, by propidium iodide incorporation and flow cytometry analysis we found an increase in the proportion of cells in G0/G1 phase and a concomitant decrease in S phase cells (Fig. 4D). Accordingly, piRNA pathway depletion did not lead to apoptosis (Fig. S3), whereas we found that it led to altered expression of genes previously associated with senescence-induced cell cycle exit (Fig. 4E, F), circadian mechanism and oxidative stress (Fig. S3), as previously reported (Adusumilli et al., 2021; Babcock et al., 2021; Schouten et al., 2020). To corroborate this evidence *in vivo*, we quantified the expression of *Mili* transcript in sorted *Nestin*-GFP⁺ NSCs from the DG of young (6 Weeks) and ~12 Months old mice (i.e., when the majority of hippocampal aNSCs turn into an aged phenotype (Martín-Suárez et al., 2019)) and found that *Mili* transcript was reduced in aged aNSCs (Fig. 4G). These results suggest that the piRNA pathway prevents aNPCs/neuroblasts senescence.

The piRNA pathway modulates noncoding RNAs and mRNAs involved in ribosome assembly and translation.

Next, we sought to identify piRNA pathway targets in aNPCs lineages (Fig.5). In contrast to germline piRNAs which primarily target TEs, somatic piRNAs have also homology with, or pair by sequence complementarity to noncoding RNAs, such as transfer RNAs (tRNAs) (Keam et al., 2014) and others (Rojas-Ríos and Simonelig, 2018). We searched for noncoding RNAs that are putative targets of the piRNAs expressed in our model (Fig. 2). Indeed, TEs were just a minor percentage of the predicted noncoding RNA targets in both undifferentiated aNPCs and progeny (Fig.5 A, B), despite their proportion being increased upon induction of neurogenesis (Fig. 5 B). The latter finding is in agreement with the observed activation of TEs (i.e., LINE1) during neuronal differentiation (Coufal et al., 2009; Muotri et al., 2005). Interestingly, 5S ribosomal RNA (5S rRNA) and tRNAs were the main predicted piRNA targets in both undifferentiated (47% and 40%, respectively) and progeny (35% and 16%, respectively, Fig. 5 A, B). To ascertain whether these noncoding RNAs are modulated by the piRNA pathway, we quantified their expression in aNPCs and progeny, upon *Mili*-KD (Fig. 5 C, D). Indeed, piRNA pathway depletion significantly elevated levels of 5S rRNA and SINE-B1 family of TEs in both undifferentiated aNPCs and progeny, compared to scrambled control (Fig.5 C), whereas LINE1, here quantified with a qPCR assay detecting the full-length transcript, was initially refractory to piRNA depletion and its level only increased late in differentiation (Fig. 5 D). These results indicate that 5s rRNAs and SINE-B1 are repressed by the piRNA pathway in neurogenesis. To

identify which mRNAs are modulated by the piRNA pathway in neurogenesis, we analyzed mRNA transcriptome by RNA seq from Mili KD or scrambled control cells during their spontaneous differentiation at DIF 4, *i.e.*, when the piRNAs are most abundant (Fig. 2). Most of the modulated genes upon piRNA pathway depletion were upregulated (Fig 5 E), and the majority of them bore sequences antisense to a piRNA (*i.e.*, were predicted piRNA targets), or harbored homologous sequences to piRNAs (Fig. 5 F). We found that mRNA transcripts from individual genes are targeted by multiple piRNAs, with a maximum of 11,904 unique piRNA sequences targeting a modulated gene (Fig. 5G). Spearman analysis indicated a positive correlation between piRNA levels in undifferentiated and differentiating aNPCs/neuroblasts, and the degree of target upregulation upon piRNA pathway depletion (Fig. 5H). Gene ontology (GO) analysis of the upregulated piRNA targets in Mili KD cells at DIF 4 indicated a prevalence of “mRNA processing” and “Translation” among the top ten biological processes affected (Fig. 5 I). Moreover “Ribosome” (p-value 7,7 E-8) and “Spliceosome” (p-value 3,3 E-7) were the top enriched pathways based on function in the Kyoto Encyclopedia of Genes and Genomes (KEGG) database (*not shown*). This evidence is consistent with our observation that 5S rRNA, SINEB1 and possibly tRNAs are modulated by the piRNA pathway in these cells.

Inhibition of the piRNA pathway in aNPCs enhances polysome assembly and results in higher protein synthesis upon differentiation.

As dysregulation of ribosome biogenesis and translation have been associated to cellular senescence (Liu and Sabatini, 2020), we analyzed polyribosomes in aNPCs and in their progeny. To this end we first used stimulated emission depletion (STED) nanoscopy, a method that allows to visualize and quantify polysome density (Viero et al., 2015). Depletion of the piRNA pathway increased polyribosomes in both undifferentiated and differentiating aNPCs, as revealed by immunostaining for the ribosomal protein RPL26, compared to control cells (Fig. 6A, B). As the density of ribosomes over transcript does not necessarily correlate with its translation (Mills and Green, 2017), we also quantified protein synthesis rate by OPP (O-propargyl-puromycin) labelling of nascent proteins during neurogenesis. Accordingly, protein synthesis rate was significantly increased upon piRNA pathway depletion in differentiating cells, but not in undifferentiated aNPCs (Fig. 6C, DIF 7). In sum, these results support a role for the piRNA pathway in sustaining adult neurogenesis by repressing translation and senescence in aNPCs.

231 Discussion

232 In this study, we investigated the expression of Mili and Mili-dependent piRNAs in mouse and human NPCs,
 233 and inferred functions of this pathway in the regulation of neurogenesis in the adult mouse hippocampus.
 234 Our results provide evidence of an essential role for the piRNA pathway in mammalian neurogenesis. This
 235 finding adds a new layer of complexity to the understanding of adult brain plasticity and aging, and entails
 236 crucial implications for neuronal disorders where dysregulated expression of the piRNA pathway has been
 237 reported, such as neurodegeneration (Jain et al., 2019; Wakisaka, 2019).
 238 Differently to the canonical functions of the piRNA pathway in germline, which are mainly required for
 239 maintenance of stem cell pools, here we provide the first evidence of a requisite role linking the piRNA
 240 pathway with proper differentiation and fate choice of neural stem cells. Specifically, we show that piRNA
 241 pathway inhibition in aNPCs leads to aberrant neurogenesis, and to an increased generation of reactive
 242 astrocytes, a phenotype which has been observed in the hippocampi of aged mice (Bonaguidi et al., 2011;
 243 Clarke et al., 2018; Encinas et al., 2011; Martín - Suárez et al., 2019). Accordingly, we find that inhibition of
 244 piRNA biogenesis in aNPCs results in senescence-like phenotype, thus providing a possible cellular
 245 mechanism that drives aNPC fate adrift toward reactive astrocytes.
 246 Moreover, and in agreement with previous observations linking cell senescence to altered ribosome
 247 biogenesis (Liu and Sabatini, 2020), our data suggest pleiotropic functions of the Mili and Mili-dependent
 248 piRNAs in aNPCs reduce polysome assembly and protein synthesis. This result differs from previous
 249 functional evidence for the piRNA pathway in germline stem cells, where Miwi/Maelstrom interacting
 250 piRNAs activate translation to sustain spermiogenesis (Castañeda et al., 2014; Dai et al., 2019).
 251 Despite the precise cascade of events that lead to dysregulation of NSCs homeostasis in aging is only
 252 beginning to emerge, proper control of proteostasis, pro-neurogenic, cell cycle and pro-inflammatory
 253 signaling is involved in maintenance of lifelong neurogenesis. Our study about Mili and its targets in mouse
 254 NSCs certainly provides an entry point to dissect the role of the piRNA pathway in mammalian neurogenesis
 255 in the context of brain aging.

256 **Methods**

257 **Lead contact and materials availability:**

258 Further information and requests for resources and reagents should be directed to and will be fulfilled by the
259 Lead Contact, Davide De Pietri Tonelli (davide.depietri@iit.it).

260 **Materials and Methods**

261 **Mice**

262 C57BL/6 and Td-Tomato^{flox/wt} knock-in reporter mice (Jackson Laboratory stock number 007908) (Madisen
263 et al., 2010), were housed at *Istituto Italiano di Tecnologia* (IIT); Nestin-GFP mice (Mignone et al., 2004) for
264 the Kainic Acid experiments were housed at the Swammerdam Institute for Life Sciences, University of
265 Amsterdam. All animal procedures were approved by IIT animal use committee and the Italian Ministry of
266 health, or by the Commission for Animal Welfare at University of Amsterdam (DEC protocol 4925,
267 AVD1110020184925), respectively and conducted in accordance with the Guide for the Care and Use of
268 Laboratory Animals of the European Community Council Directives. All mice were group-housed under a 12-
269 h light-dark cycle in a temperature and humidity-controlled environment with ad libitum access to food and
270 water.

271 **aNPCs cultures**

272 Hippocampal NPCs were prepared and expanded as described previously (Babu et al., 2011; Pons-Espinal et
273 al., 2019; Walker and Kempermann, 2014) and induction of spontaneous differentiation by growth factor
274 removal was done as previously described (Pons-Espinal 2017, and Pons-Espinal, Gasparini et al 2019); viral
275 induced-neuronal differentiation of aNPCs was done by transduction of a viral construct expressing Ascl1-
276 ERT2 as previously described (Braun et al., 2013).

277 **Protein extraction and Western blot**

278 For total protein extraction, adult testes or hippocampus or cell pellets were homogenized in RIPA buffer and
279 the protein concentration was determined using a Bradford Assay kit (Bio-Rad). For blot analysis, equal
280 amounts of protein (30 µg) were run on homemade 10% polyacrylamide gels and transferred on nitrocellulose
281 membranes (GE Healthcare). Membranes were probed with primary antibodies (listed in the table below),
282 followed by HRP-conjugated secondary antibody anti-rabbit or mouse (Invitrogen, A16104, A16072; 1:2,000).

The band corresponding to Mili protein was detected with two different antibodies and validated with four different RNAi constructs (1 shRNA virus and 3 GapmeRs). LAS 4000 Mini Imaging System (GE Healthcare) was used to digitally acquire chemiluminescence signals, and the band intensities were quantified using Fiji (Macbiophotonics, Fiji is Just ImageJ) (Schindelin et al., 2012). List of antibodies used available in the SI appendix.

Virus and GapmeR injection

Virus or GapmeR injection was done as previously shown (Pons-Espinal et al., 2019): 8 weeks-old mice Td-Tomato^{flox/wt} or WT C57BL6/J were anesthetized with isoflurane, 1 µl of virus mix (Split-Cre N-Cre:C-Cre) or 1.5 µl of antisense LNA GapmeR for Mili-KD or negative control (MILI 339511, Control 339515, Qiagen), were stereotactically injected in the dentate gyrus. To assess the efficacy of *Mili* knockdown, a first group of mice (n=5) was sacrificed 48 hours after the injection and the DG dissected for RNA or protein extraction. 24 hours after the oligos injection another set of animals received 2 BrdU intraperitoneal injections per day for 5 days (50 mg/kg) (one every 12 hours). Animals were sacrificed 10 (n=5) or 30 days after oligos injection (n=7) for histological analysis, as previously described (Pons-Espinal et al., 2019). Mice were anesthetized with intraperitoneal administration of ketamine (90mg/kg) and xylazine (5-7mg/kg), and subsequently perfused with PBS followed by 4% paraformaldehyde (PFA). Brains were harvested, postfixed overnight in 4% PFA, and then equilibrated in 30% sucrose. 40 µm brain sections were generated using a sliding microtome and were stored in a -20°C freezer as floating sections in 48 well plates filled with cryoprotectant solution (glycerol, ethylene glycol, and 0.2 M phosphate buffer, pH 7.4, 1:1:2 by volume). Slices were used for immunofluorescence and immunohistochemical analysis.

Fluorescence-Activated Cell Sorting (FACS) and flow cytometric analysis of cell cycle distribution

For RNA extraction and cDNA preparation, Td-Tomato^{flox/wt} or Nestin-GFP mice were used. Six to ten Td-Tomato^{flox/wt} mice were euthanized 10 or 30 days after the split cre viruses injection. DG cells were dissociated with the Neural Tissue Dissociation Kit P (Miltenyi Biotec) and FACS-sorted as previously published (Walker et al., 2016). FACS-sorted cells were immediately processed for RNA extraction. To measure the cell cycle length, we used propidium iodide (PI), which binds to DNA by intercalating between the bases, as previously described (Krishan). Briefly, cells were trypsinized, resuspended in PBS and fixed

with 70% of ethanol for 40 minutes on ice. Cells were then centrifuged, resuspended in PBS for 15 minutes and then incubated 1h at 37°C with 60 µg/ml of PI (Sigma). Cells were collected by centrifuge and resuspended in ice-cold PBS for FACS analysis.

Immunostaining analysis

The immunostaining on brain slices was performed on sections covering the entire dorsal hippocampus as previously described (Paxinos, 2001; Pons-Espinal et al., 2019). To detect Ki67 staining, citrate buffer 10 mM pH = 6 treatment during 10 min at 95 °C was used. Primary antibodies are listed below, secondary fluorescent antibodies were diluted 1:1000 (Goat Alexa 488, 568, and 647nm, Invitrogen). Confocal stack images of brain slices (40µm) were obtained with the Confocal A1 Nikon Inverted SFC with 20x objective. Cell quantification and analysis was performed using NIS-Elements software (Nikon) and the Cell-counter plugin in Fiji. Immunofluorescence staining on cell cultures was performed as reported in (Pons-Espinal et al., 2019). To detect BrdU incorporation, cells were pretreated with 2N HCl for 30 min at 37°C. Cells were mounted in mounting medium and counterstained with fluorescent nuclear dye DAPI (Invitrogen). Images were obtained using the microscope Nikon Eclipse at 20x or 40x magnification and quantification was performed using a Cell-counter plugin in Fiji. DAB staining was performed as previously reported (Bielefeld et al., 2019). Briefly, sections were incubated with peroxidase block (Vectashield), permeabilized with 0.3% PBS-Triton X (PBS-T) and 0.1% PBS-T. Sections were blocked with 0.1% PBS-T and 5% Normal Goat Serum (NGS), incubated with primary antibodies and subsequently with the corresponding biotinylated secondary antibodies (1:1000 Goat anti-rabbit, Invitrogen). Signal amplification was performed using the ABC complex (Vectashield), according to manufacturer's instructions. Sections were incubated with the solution for DAB reaction (Sigma) and counterstained with Hoechst (1:300), mounted and cover slipped with Vectashield reagent (VECTOR Labs). List of antibodies used available in the SI Appendix.

RNA extraction and real time qPCR

Total RNA was extracted from aNPCs (proliferating and differentiating conditions), or DG dissected from adult C57BL/6, Nestin-GFP or Td-Tomato^{flox/wt} mice with QIAzol protocol (Qiagen) according to the manufacturer's instructions. 1 µg of total RNA was treated with DNase I (Sigma) and cDNA was synthesized using iScript cDNA Synthesis kit (Bio-Rad) or with ImProm-II reverse transcriptase (Promega). Real time qPCR was performed in duplex with Actin or Ubiquitin C as a reference gene, with QuantiFast SYBR Green

339 PCR Kit (Qiagen) or Taqman Assay (Thermo Fisher) on ABI-7500 Real-Time PCR System (Applied
340 Biosystems). Expression levels were determined relative to Ubiquitin C or Actin, using delta delta Ct method.
341 Primers listed below were designed using NCBI/UCSC Genome Browser and Primer3 software tools and then
342 checked in PrimerBLAST for their specificity to amplify the desired genes. List of primers used available in
343 the SI Appendix.

344 **Small RNA library preparation**

345 Cells were lysed in QIAzol lysis reagent and total RNA was isolated using the miRNeasy Mini kit (Qiagen),
346 according to the manufacturer's instructions. Quantity and quality of the total RNA were measured by
347 Nanodrop spectrophotometer and Experion RNA chips (Bio-Rad). RNA with RNA integrity number (RIN)
348 values ≥ 9.5 were selected for the study. 1 μ g of high-quality RNA for each sample was used for library
349 preparation according to the Illumina TruSeq small RNA library protocol (Illumina Inc., CA). Briefly, 3'
350 adapters were ligated to 3' end of small RNAs using a truncated RNA ligase enzyme followed by 5' adaptor
351 ligation using RNA ligase enzyme. Reverse transcription followed by PCR was used to prepare cDNA using
352 primers specific for the 3' and 5' adapters. The amplification of those fragments having adapter molecules on
353 both ends was carried out with 13 PCR cycles. The amplified libraries were pooled together and run on a 6%
354 polyacrylamide gel. The 145-160 bp bands (which correspond to inserts of 24-32 nt cDNAs) were extracted
355 and purified using the Wizard® SV Gel and PCR Clean-Up System (Promega). The quality of the library was
356 assessed by the Experion DNA 1K chips (Bio-Rad). Small RNA sequencing using HiSeq2000 (Illumina Inc.,
357 CA) was performed by the Center for Genomic Science of IIT@SEMM.

358 **Mili knock down *in vitro***

359 To constitutively knockdown Mili expression *in vitro*, aNPCs were infected at MOI=5 with a lentivirus
360 encoding for a *Mili*-targeted short hairpin (shMILI, pKO.1, Sigma), or for a short hairpin scramble lentivirus
361 (Control, SHC202, Sigma) both decorated with an eGFP reporter. GFP-positive cells were first selected by
362 FACS after three passages, and then plated in proliferating or differentiating media, as previously described.
363 We also performed the knock down using two different synthetic antisense LNA GapmeRs for Mili-KD or
364 negative control (Mili 339511, Control 339515, Qiagen). Mili knock down was assessed by real time qPCR
365 and Western Blot.

366 **mRNA library preparation**

aNPCs WT and transduced with the Control or with the shMILI lentiviruses, were grown to confluence and allowed to spontaneously differentiate for the indicated days. Total RNA was extracted using QIAzol lysis reagent and quantity and quality of the total RNA were measured by Qubit 4 Fluorometer (Thermo Fisher) and Bioanalyzer RNA chips (Agilent). RNA with RNA integrity number (RIN) values ≥ 8 were selected for the study. 30 ng of high-quality RNA for each sample was used for library preparation according to the Illumina Stranded Total RNA Prep, Ligation with Ribo-Zero Plus Kit (20040529, Illumina Inc., CA) using the IDT for Illumina Indexes Set A (20040553). Briefly, after ribosomal RNA depletion, RNA was fragmented and denatured and cDNA synthesized. Then the 3' ends were adenylated, and anchors ligated. After amplification and clean up, quality of the libraries was assessed by the Bioanalyzer DNA chips (Agilent). Paired-End stranded total RNA sequencing on NovaSeq 6000 Sequencing System instrument (Illumina Inc., CA), was performed by the IIT Genomic Unit @Center for Human Technologies.

Small RNA sequencing data processing

Illumina reads were trimmed to remove the 3' adapter using Cutadapt, with parameters -m 25 -q 20. Since piRNA size ranges from 26 to 31 bases, all sequences with length ≤ 24 bases were discarded. Reads mapped to known non-coding RNAs (RNAcentral v6.0 snoRNA, UCSC tRNA, miRBase Release 21 miRNA hairpin and mature miRNA annotation, NCBI complete ribosomal DNA unit) (Karolchik, 2004; Kozomara and Griffiths-Jones, 2014; Petrov et al., 2015) were removed from the datasets. The comparison was performed using NCBI BLASTN v2.6.0 with parameters -max_hsps= 1, -max_target_seqs= 1, -perc_identity= 80, mismatches ≤ 1 , qcovhsp ≥ 90 (Altschul et al., 1990). Reads were aligned on the non-repeat-masked UCSC release 9 of the mouse genome (MM9) (Waterston et al., 2002) using bowtie2 (Langmead and Salzberg, 2012) v2.2.6 with the sensitive preset option and allowed a maximum of 100 alignments. All the reads that aligned to the genome were retained and used for subsequent analysis. piRNA clusters were identified collapsing overlapped piRNA sequences (piRBase Release 1) (Zhang et al., 2014) into one cluster (mergeBed with preset options) (Quinlan and Hall, 2010). piRNA clusters and all the reads that aligned to the genome were intersected (intersectBed with option -f 1). Intersection files were then parsed using a custom perl script in order to evaluate alignment counts. Differential expression was assessed using DESeq2 (Love et al., 2014). piRNA clusters were considered differentially expressed when the adjusted p-value was ≤ 0.05 , and down- and up-regulation was established in the range of ≤ -1 to ≥ 1 log2 fold-change,

395 respectively. piRNA sequences were then categorized for the putative mRNA transcript targets (for each gene).
 396 In order to obtain a count of piRNA target levels which target individual gene transcripts, for each
 397 differentiation time-point (DIF0-7), piRNA transcripts were expressed in transcripts per million (TPM), and
 398 summed for each target category. Spearman correlation was performed between the levels of the piRNA in the
 399 Sh-Scramble (control) genotype, and compared to the fold-change level of the putative target genes which
 400 were found to be significantly altered (up and down) in the Sh-Mili-KD genotype. In order to assess the
 401 clustering behavior of putative piRNAs, the 5' termini positions of each cluster-associated putative primary
 402 and putative secondary piRNA sequences were analyzed for distance, represented as probability within a range
 403 of 200 nucleotides in the 5' direction and 200 nucleotides in the 3' direction of the putative primary piRNAs,
 404 as reported previously (Gainetdinov et al., 2018). The positional distance between piRNAs for each cluster
 405 was sampled iteratively and normalized by the total number of diverse piRNAs associated with each cluster.
 406 The distance probability distribution was assayed by the locally weighted smoothing linear regression method
 407 (LOWESS), by using the built-in MATLAB 'fit' function (MathWorks, Natick, MA), with a span value of 0.1.

408 **mRNA Sequencing data processing**

409 Illumina sequencing was performed bidirectionally, and in duplicate by two flowcell pairs of 100 and 150 base
 410 pairs, for a total of 6 measurements produced from 3 independent samples for each differentiation time-point
 411 and genotype. Adapter sequences were trimmed using *Cutadapt*, after which a quality control trim was
 412 implemented on a sliding window of 25 nucleotides, for 2 base pairs with a minimum quality score of 26, with
 413 the *Bowtie* build for the MATLAB bioinformatics suite (MathWorks, Natick, MA). Transcript quantification
 414 was performed with the *Salmon* suite, as reported previously (Patro et al., 2017), on the NCBI mouse genome,
 415 release 67, obtained from the ENSEMBL FASTA directory. The identified ENSEMBL gene accessions were
 416 grouped for the different transcript reads, and the read counts, expressed in TPM, were summed for the
 417 annotated transcripts. Outlier reads for each gene transcript level in TPM were detected by the mean absolute
 418 deviations method (MAD), where reads with more than 3 scaled MAD distances from the mean were
 419 eliminated from statistical analysis. Then, the mean and SD for each gene were used for statistical analysis
 420 among the different genotypes by one-way ANOVA with multiple comparison. *P*-values lower than, or equal
 421 to, 0.05 were selected as the threshold of significance, for a minimum count of 4 of 6 samples per gene.
 422 Database for Annotation, Visualization and Integrated Discovery (DAVID, <https://david.ncifcrf.gov/>), (Huang

et al., 2009), was used to perform Gene ontology (GO) and Kyoto Encyclopedia of Genes and Genomes (KEGG) signaling pathway analysis.

Periodate oxidation and alkaline β -elimination

Periodate oxidation and alkaline β -elimination was performed as previously described (Balaratnam et al., 2018). Briefly, total small RNAs were isolated using miRNeasy Mini kit (Qiagen) according to the manufacture's protocol. Each sample was split in two portions, each containing 25 μ g of RNA and independently treated with either 200 mM of sodium periodate or water, and RNA precipitated by ethanol. As internal control for the assay, a synthetic piRNA sequence (corresponding to one of the most abundant piRNA found in aNPCs – piR-cluster-1) either modified with the 3'-end 2'-O-methylation (positive control) or bearing a terminal 2',3'-hydroxyl group (negative control) were subject to the periodate treatment as above. The samples and control oligos were finally quantified by qPCR-TaqMan small RNA assay.

piRNAs real time qPCR

Total RNA enriched in the fraction of small RNAs, was extracted using miRNeasy Mini kit following the manufacturer's instructions from aNPCs, DG extracted from C57BL6/J or Td-Tomato^{flox/wt} mice. cDNA was obtained using the TaqMan MicroRNA Reverse Transcription Kit (Thermo Fisher) according to the manufacturer's instructions and quantified using the Custom TaqMan Small RNA Assay (Thermo Fisher) on a ABI-7500 Real-Time PCR System (Applied Biosystems). Each sample was normalized to U6 snRNA level (Thermo Fisher). Cluster sequences used for probe design are listed in Table S1.

β -galactosidase detection

Was obtained with the Senescence Cells Histochemical Staining Kit (Sigma-Aldrich, CS0030), according the manufacturer's instructions. Briefly, cells were plated on coverslip in proliferating medium. 48h after the induction of spontaneous differentiation, cells were washed twice with PBS 1X and incubated with Fixation Buffer 1X for 7 min at RT. Next, cells were rinsed with PBS 1X and incubated with fresh senescence-associated β -Gal (SA- β -Gal) stain solution at 37°C (no CO₂) for 4 h. Reaction was blocked with PBS 1X and coverslips were mounted on slides using Vectashield reagent (VECTOR Labs). Images were obtained using the microscope Nikon Eclipse, the percentage of cells expressing β -galactosidase was quantified over the number of total cells using a Cell-counter plugin in Fiji software.

450 ***in silico* piRNA targets prediction**

451 For piRNA targets analysis, we divided the sequencing data in one set of 100 piRNA clusters enriched in
 452 proliferating aNPCs (DIF0) and a second set of 198 clusters specifically expressed at DIF4/7 stage.
 453 The Differential Expression analysis for piRNAs mapping on REs showing trends for enrichment of piRNAs
 454 mapping on repeat elements (REs) in DIF4 and DIF7 compared to DIF0 was done using EdgeR software
 455 package (Robinson and Oshlack, 2010). Identification of piRNA targets was divided in: piRNAs mapping on
 456 REs only / piRNAs mapping on GENCODE elements / piRNAs mapping on REs within GENCODE
 457 elements / unannotated piRNAs / piRNAs clusters. Gene Ontology analysis for piRNAs mapping on
 458 GENCODE protein-coding genes (but NOT mapping on REs) has been done with the R package GOfuncR
 459 (<https://bioconductor.org/packages/release/bioc/html/GOfuncR.html>)

460 **Protein synthesis assay**

461 To quantify the protein synthesis rate of cells, we used the Global Protein Synthesis Assay Kit
 462 (FACS/Microscopy), Red Fluorescence kit (abcam), following the manufacturer's instructions. Briefly, cells
 463 in proliferating or differentiating media (DIF7) were treated with Cycloheximide as an inhibitor of protein
 464 synthesis, for 30 min at 37°C. Media were replaced with fresh aliquots containing Protein Label (400X)
 465 diluted to 1X final concentration and the cells were incubated for additional 30 min at 37°C. Negative
 466 control cells were not incubated with the protein label. Samples were analyzed by FACS for red fluorescence
 467 generated by *de novo* synthesized protein during click reaction. Translation rate is directly proportional to
 468 emitted fluorescence. Cells emitting fluorescence lower than 10^3 were considered negative (P3), higher than
 469 10^4 were considered positive (P2).

470 **Kainic Acid Administration, single cell suspension and enrichment of aNPCs by FACS**

471 Kainic Acid to elicit tonic, non-convulsive epileptic seizures, was administered as described before (Bielefeld
 472 et al., 2019). Briefly, 50nL of 2.22mM Kainic Acid dissolved in PBS (pH 7.4) was injected bilaterally into the
 473 hippocampus at the following coordinates (AP -2.0, ML +/- 1.5, DV -2.0 mm) (between 9AM and 1PM).
 474 Control animals were administered saline (pH 7.4). Bilateral dentate gyri from 3 animals per condition were
 475 pooled to allow sufficient recovery of NPCs. A single cell suspension was created using a Neural Tissue
 476 Dissociation kit (Miltenyi Biotec), according to the manufacturers protocol. In order to enrich aNPCs from the
 477 DG, we used the endogenous GFP expression driven by the Nestin promotor in combination with FACS.

Propidium Iodide (5µg/mL) was added to the single cell suspension to assess cell viability. Cells were sorted using a FACS Aria III system (BD) with 488nm excitation laser. Cell duplets were removed based on forward and side scatter and viable cells were selected based on PI negativity. GFP-positive (corrected for autofluorescence) cells were sorted (\cong 50000 cells/pool) and collected in PBS containing 1% FBS. Trizol LS (Thermo Scientific) was added and after resuspension samples were snap-frozen and stored at -20°C.

Immunofluorescence, STED nanoscopy and particle analysis

Confocal and Stimulated Emission Depletion (STED) nanoscopy were performed as previously reported (Diaspro and Bianchini, 2020; Vicidomini et al., 2018). aNPCs were plated on glass coverslips 24 h before fixation. Cells were fixed with PFA 4%, permeabilized with PBS-T 0.1%, blocked 1 hour at room temperature with PBS-T 0.1% NGS 5% and incubated according to the dilution suggested by the manufacturer's instructions with 0.01 µg/ml rabbit polyclonal antibody against the N terminus of RPL26 (Abcam) for 1 h at room temperature. Cells were washed extensively and incubated with the secondary antibody goat anti-rabbit ATTO-647N (0.8 µg/ml; Sigma) for 45 min. Nuclei were stained while mounting the coverslip with DAPI-Prolong antifade (Invitrogen). Confocal and STED images were acquired at 23°C with a modified TCS SP5 STED-CW gated (Leica Microsystems, Mannheim, Germany) operated with Leica's microscope imaging software. The microscope has been customized with a second pulsed STED laser line at 775nm. The beam originates from a OneFive Katana HP 8 (NKT, Birkerød, Denmark) and pass through a vortex phase plate (RPC photonics, Rochester, NY, USA) before entering the microscope through the IR port. The depletion laser pulses are electronically synchronized with the Leica's supercontinuum pulsed and visible excitation laser. The ATTO- 647N fluorescence was excited at 633 nm, and the fluorescence depletion was performed 775 nm. The maximal focal power of the STED beam was 200 mW at 80 MHz. Both beams were focused into the 1.4 NA objective lens (HCX PL APO 100× 1.40 NA Oil STED Orange; Leica). Fluorescence was collected by the same lens, filtered with a 775 nm notch filter, and imaged in the spectral range 660–710 nm by hybrid detector with a time gating of 1 ns. All of the images have 14-nm pixel size and 37-µs pixel dwell time. We performed the analysis of polysome clusters in aNPCs on more than 20 images likewise different cells. Image analysis was performed using the Fiji software.

Quantification and Statistical analysis

505 Data are presented as mean \pm SEM and were analyzed using Prism 6 (GraphPad). Statistical significance was
 506 assessed with a two-tailed unpaired t test for two experimental groups. For experiments with three or more
 507 groups, one-way ANOVA with Bonferroni's multiple comparison test as post hoc was used. Results were
 508 considered significant when $p < 0.05$.

509 **Data and code availability**

510 RNA sequencing data (mouse) have been deposited in the European Nucleotide Archive (ENA) at EMBL-EBI
 511 and available upon request; human datasets are available through RIKEN FANTOM5.

512

513 **References**

- 514 Adusumilli, V.S., Walker, T.L., Overall, R.W., Klatt, G.M., Zeidan, S.A., Zocher, S., Kirova, D.G., Ntitsias,
515 K., Fischer, T.J., Sykes, A.M., et al. (2021). ROS Dynamics Delineate Functional States of Hippocampal
516 Neural Stem Cells and Link to Their Activity-Dependent Exit from Quiescence. *Cell Stem Cell* 28, 300-
517 314.e6.
- 518 Altman, J. (1962). Are new neurons formed in the brains of adult mammals? *Science* (80-.). 135, 1127–
519 1128.
- 520 Altschul, S.F., Gish, W., Miller, W., Myers, E.W., and Lipman, D.J. (1990). Basic local alignment search
521 tool. *J. Mol. Biol.* 215, 403–410.
- 522 Aravin, A., Gaidatzis, D., Pfeffer, S., Lagos-Quintana, M., Landgraf, P., Iovino, N., Morris, P., Brownstein,
523 M.J., Kuramochi-Miyagawa, S., Nakano, T., et al. (2006). A novel class of small RNAs bind to MILI protein
524 in mouse testes. *Nature* 442, 203–207.
- 525 Babcock, K.R., Page, J.S., Fallon, J.R., and Webb, A.E. (2021). Adult hippocampal neurogenesis in aging
526 and Alzheimer’s disease. *Stem Cell Reports*.
- 527 Babu, H., Claasen, J.H., Kannan, S., Rünker, A.E., Palmer, T., and Kempermann, G. (2011). A protocol for
528 isolation and enriched monolayer cultivation of neural precursor cells from mouse dentate gyrus. *Front.*
529 *Neurosci.* 5, 89.
- 530 Balaratnam, S., West, N., and Basu, S. (2018). A piRNA utilizes HILI and HIWI2 mediated pathway to
531 down-regulate ferritin heavy chain 1 mRNA in human somatic cells. *Nucleic Acids Res.* 46, 10635–10648.
- 532 Beckervordersandforth, R., Deshpande, A., Schäffner, I., Huttner, H.B., Lepier, A., Lie, D.C., and Götz, M.
533 (2014). In vivo targeting of adult neural stem cells in the dentate gyrus by a Split-Cre Approach. *Stem Cell*
534 *Reports* 2, 153–162.
- 535 Bielefeld, P., Sierra, A., Encinas, J.M., Maletic-Savatic, M., Anderson, A., and Fitzsimons, C.P. (2017). A
536 Standardized Protocol for Stereotaxic Intrahippocampal Administration of Kainic Acid Combined with
537 Electroencephalographic Seizure Monitoring in Mice. *Front. Neurosci.* 11.
- 538 Bielefeld, P., Schouten, M., Meijer, G.M., Breuk, M.J., Geijtenbeek, K., Karayel, S., Tiaglik, A., Vuuregge,
539 A.H., Willems, R.A.L., Witkamp, D., et al. (2019). Co-administration of anti microRNA-124 and -137
540 oligonucleotides prevents hippocampal neural stem cell loss upon non-convulsive seizures. *Front. Mol.*

Neurosci. *12*.

Bonaguidi, M.A., Wheeler, M.A., Shapiro, J.S., Stadel, R.P., Sun, G.J., Ming, G.-L., and Song, H. (2011). In Vivo Clonal Analysis Reveals Self-Renewing and Multipotent Adult Neural Stem Cell Characteristics. *Cell* *145*, 1142–1155.

Braun, S.M.G., Machado, R.A.C., and Jessberger, S. (2013). Temporal Control of Retroviral Transgene Expression in Newborn Cells in the Adult Brain. *Stem Cell Reports* *1*, 114–122.

Castañeda, J., Genzor, P., Heijden, G.W., Sarkeshik, A., Yates, J.R., Ingolia, N.T., and Bortvin, A. (2014). Reduced pachytene piRNA s and translation underlie spermiogenic arrest in Maelstrom mutant mice. *EMBO J.* *33*, 1999–2019.

Clarke, L.E., Liddelow, S.A., Chakraborty, C., Münch, A.E., Heiman, M., and Barres, B.A. (2018). Normal aging induces A1-like astrocyte reactivity. *Proc. Natl. Acad. Sci.* *115*, E1896–E1905.

Coufal, N.G., Garcia-Perez, J.L., Peng, G.E., Yeo, G.W., Mu, Y., Lovci, M.T., Morell, M., O’Shea, K.S., Moran, J. V., and Gage, F.H. (2009). L1 retrotransposition in human neural progenitor cells. *Nature* *460*, 1127–1131.

Czech, B., Munafò, M., Ciabrelli, F., Eastwood, E.L., Fabry, M.H., Kneuss, E., and Hannon, G.J. (2018). piRNA-Guided Genome Defense: From Biogenesis to Silencing. *Annu. Rev. Genet.* *52*, 131–157.

Dai, P., Wang, X., Gou, L.T., Li, Z.T., Wen, Z., Chen, Z.G., Hua, M.M., Zhong, A., Wang, L., Su, H., et al. (2019). A Translation-Activating Function of MIWI/piRNA during Mouse Spermiogenesis. *Cell* *179*, 1566–1581.e16.

Diaspro, A., and Bianchini, P. (2020). Optical nanoscopy. *Riv. Del Nuovo Cim.* 1–71.

Doetsch, F., Caille, I., Lim, D.A., Garcia-Verdugo, J.M., and Alvarez-Buylla, A. (1999). Subventricular zone astrocytes are neural stem cells in the adult mammalian brain. *Cell* *97*, 703–716.

Encinas, J.M., Michurina, T. V., Peunova, N., Park, J.H., Tordo, J., Peterson, D.A., Fishell, G., Koulakov, A., and Enikolopov, G. (2011). Division-coupled astrocytic differentiation and age-related depletion of neural stem cells in the adult hippocampus. *Cell Stem Cell* *8*, 566–579.

Escartin, C., Galea, E., Lakatos, A., O’Callaghan, J.P., Petzold, G.C., Serrano-Pozo, A., Steinhäuser, C., Volterra, A., Carmignoto, G., Agarwal, A., et al. (2021). Reactive astrocyte nomenclature, definitions, and future directions. *Nat. Neurosci.* *24*, 312–325.

Gainetdinov, I., Colpan, C., Arif, A., Cecchini, K., and Zamore, P.D. (2018). A Single Mechanism of Biogenesis, Initiated and Directed by PIWI Proteins, Explains piRNA Production in Most Animals. *Mol. Cell* 71, 775-790.e5.

Ghosheh, Y., Seridi, L., Ryu, T., Takahashi, H., and Orlando, V. (2016). Characterization of piRNAs across postnatal development in mouse brain. *Nat. Publ. Gr.* 1–7.

Girard, A., Sachidanandam, R., Hannon, G.J., and Carmell, M.A. (2006). A germline-specific class of small RNAs binds mammalian Piwi proteins. *Nature* 442, 199–202.

Huang, D.W., Sherman, B.T., and Lempicki, R.A. (2009). Systematic and integrative analysis of large gene lists using DAVID bioinformatics resources. *Nat. Protoc.* 4, 44–57.

Huang, H., Yu, X., Han, X., Hao, J., Zhao, J., Bebek, G., Bao, S., Prayson, R.A., Khalil, A.M., Jankowsky, E., et al. (2021). Piwil1 Regulates Glioma Stem Cell Maintenance and Glioblastoma Progression. *Cell Rep.* 34, 108522.

Jain, G., Stuendl, A., Rao, P., Berulava, T., Pena Centeno, T., Kaurani, L., Burkhardt, S., Delalle, I., Kornhuber, J., Hüll, M., et al. (2019). A combined miRNA–piRNA signature to detect Alzheimer’s disease. *Transl. Psychiatry* 9, 250.

Karolchik, D. (2004). The UCSC Table Browser data retrieval tool. *Nucleic Acids Res.* 32, 493D – 496.

Keam, S.P., Young, P.E., McCorkindale, A.L., Dang, T.H.Y., Clancy, J.L., Humphreys, D.T., Preiss, T., Hutvagner, G., Martin, D.I.K., Cropley, J.E., et al. (2014). The human Piwi protein Hiwi2 associates with tRNA-derived piRNAs in somatic cells. *Nucleic Acids Res.* 42, 8984–8995.

Kirino, Y., and Mourelatos, Z. (2007). Mouse Piwi-interacting RNAs are 2'-O-methylated at their 3' termini. *Nat. Struct. Mol. Biol.* 14, 347–348.

Kozomara, A., and Griffiths-Jones, S. (2014). MiRBase: Annotating high confidence microRNAs using deep sequencing data. *Nucleic Acids Res.* 42.

Krishan, (1975). Rapid flow cytofluorometric analysis of mammalian cell cycle by propidium iodide staining. *J. Cell Biol.* 66, 188–193.

Langmead, B., and Salzberg, S.L. (2012). Fast gapped-read alignment with Bowtie 2. *Nat. Methods* 9, 357–359.

Lee, E.J., Banerjee, S., Zhou, H., Jammalamadaka, A., Arcila, M., Manjunath, B.S., and Kosik, K.S. (2011).

597 Identification of piRNAs in the central nervous system. *Rna* 17, 1090–1099.

598 Leighton, L.J., Wei, W., Marshall, P.R., Ratnu, V.S., Li, X., Zajackowski, E.L., Spadaro, P.A., Khandelwal,
599 N., Kumar, A., and Bredy, T.W. (2019). Disrupting the hippocampal Piwi pathway enhances contextual fear
600 memory in mice. *Neurobiol. Learn. Mem.* 161, 202–209.

601 Liddelow, S.A., Guttenplan, K.A., Clarke, L.E., Bennett, F.C., Bohlen, C.J., Schirmer, L., Bennett, M.L.,
602 Münch, A.E., Chung, W.-S., Peterson, T.C., et al. (2017). Neurotoxic reactive astrocytes are induced by
603 activated microglia. *Nature* 541, 481–487.

604 Liu, G.Y., and Sabatini, D.M. (2020). mTOR at the nexus of nutrition, growth, ageing and disease. *Nat. Rev.*
605 *Mol. Cell Biol.* 21, 183–203.

606 Love, M.I., Huber, W., and Anders, S. (2014). Moderated estimation of fold change and dispersion for RNA-
607 seq data with DESeq2. *Genome Biol.* 15.

608 Madisen, L., Zwingman, T.A., Sunkin, S.M., Oh, S.W., Zariwala, H.A., Gu, H., Ng, L.L., Palmiter, R.D.,
609 Hawrylycz, M.J., Jones, A.R., et al. (2010). A robust and high-throughput Cre reporting and characterization
610 system for the whole mouse brain. *Nat. Neurosci.* 13, 133–140.

611 Martín-Suárez, S., Valero, J., Muro-García, T., and Encinas, J.M. (2019). Phenotypical and functional
612 heterogeneity of neural stem cells in the aged hippocampus. *Aging Cell* 18, e12958.

613 Mignone, J.L., Kukekov, V., Chiang, A.S., Steindler, D., and Enikolopov, G. (2004). Neural Stem and
614 Progenitor Cells in Nestin-GFP Transgenic Mice. *J. Comp. Neurol.* 469, 311–324.

615 Mills, E.W., and Green, R. (2017). Ribosomopathies: There's strength in numbers. *Science* 358, 1-8.

616 Muotri, A.R., Chu, V.T., Marchetto, M.C.N., Deng, W., Moran, J. V., and Gage, F.H. (2005). Somatic
617 mosaicism in neuronal precursor cells mediated by L1 retrotransposition. *Nature* 435, 903–910.

618 Nandi, S., Chandramohan, D., Fioriti, L., Melnick, A.M., Hébert, J.M., Mason, C.E., Rajasethupathy, P., and
619 Kandel, E.R. (2016). Roles for small noncoding RNAs in silencing of retrotransposons in the mammalian
620 brain. *Proc. Natl. Acad. Sci. U. S. A.* 113, 12697–12707.

621 Nolde, M.J., Cheng, E. chun, Guo, S., and Lin, H. (2013). Piwi Genes Are Dispensable for Normal
622 Hematopoiesis in Mice. *PLoS One* 8, 1–8.

623 Ozata, D.M., Gainetdinov, I., Zoch, A., O'Carroll, D., and Zamore, P.D. (2019). PIWI-interacting RNAs:
624 small RNAs with big functions. *Nat. Rev. Genet.* 20, 89–108.

625 Patro, R., Duggal, G., Love, M.I., Irizarry, R.A., and Kingsford, C. (2017). Salmon provides fast and bias-
626 aware quantification of transcript expression. *Nat. Methods* 14, 417–419.

627 Petrov, A.I., Kay, S.J.E., Gibson, R., Kulesha, E., Staines, D., Bruford, E.A., Wright, M.W., Burge, S., Finn,
628 R.D., Kersey, P.J., et al. (2015). RNACentral: An international database of ncRNA sequences. *Nucleic Acids*
629 *Res.* 43, D123–D129.

630 Paxinos, G. and F.K.B.J. (2001). *The Mouse Brain in Stereotaxic Coordinates*. 2nd Edition.

631 Perera, B.P.U., Tsai, Z.T.Y., Colwell, M.L., Jones, T.R., Goodrich, J.M., Wang, K., Sartor, M.A., Faulk, C.,
632 and Dolinoy, D.C. (2019). Somatic expression of piRNA and associated machinery in the mouse identifies
633 short, tissue-specific piRNA. *Epigenetics* 14, 504–521.

634 Pons-Espinal, M., de Luca, E., Marzi, M.J., Beckervordersandforth, R., Armirotti, A., Nicassio, F., Fabel, K.,
635 Kempermann, G., and De Pietri Tonelli, D. (2017). Synergic Functions of miRNAs Determine Neuronal Fate
636 of Adult Neural Stem Cells. *Stem Cell Reports* 8, 1046–1061.

637 Pons-Espinal, M., Gasparini, C., Marzi, M.J., Braccia, C., Armirotti, A., Pötzsch, A., Walker, T.L., Fabel,
638 K., Nicassio, F., Kempermann, G., et al. (2019). MiR-135a-5p Is Critical for Exercise-Induced Adult
639 Neurogenesis. *Stem Cell Reports* 12, 1298–1312.

640 Quinlan, A.R., and Hall, I.M. (2010). BEDTools: A flexible suite of utilities for comparing genomic features.
641 *Bioinformatics* 26, 841–842.

642 De Rie, D., Abugessaisa, I., Alam, T., Arner, E., Arner, P., Ashoor, H., Åström, G., Babina, M., Bertin, N.,
643 Burroughs, A.M., et al. (2017). An integrated expression atlas of miRNAs and their promoters in human and
644 mouse. *Nat. Biotechnol.* 35, 872–878.

645 Robinson, M.D., and Oshlack, A. (2010). A scaling normalization method for differential expression analysis
646 of RNA-seq data. *Genome Biol.* 11, R25.

647 Rojas-Ríos, P., and Simonelig, M. (2018). piRNAs and PIWI proteins: regulators of gene expression in
648 development and stem cells. *Development* 145, dev161786.

649 Schindelin, J., Arganda-Carreras, I., Frise, E., Kaynig, V., Longair, M., Pietzsch, T., Preibisch, S., Rueden,
650 C., Saalfeld, S., Schmid, B., et al. (2012). Fiji: an open-source platform for biological-image analysis. *Nat.*
651 *Methods* 9, 676–682.

652 Schouten, M., Bielefeld, P., Garcia-Corzo, L., Passchier, E.M.J., Gradari, S., Jungenitz, T., Pons-Espinal, M.,

653 Gebara, E., Martín-Suárez, S., Lucassen, P.J., et al. (2020). Circadian glucocorticoid oscillations preserve a
654 population of adult hippocampal neural stem cells in the aging brain. *Mol. Psychiatry* 25, 1382–1405.

655 Sharma, A.K., Nelson, M.C., Brandt, J.E., Wessman, M., Mahmud, N., Weller, K.P., and Hoffman, R.
656 (2001). Human CD34(+) stem cells express the hiwi gene, a human homologue of the Drosophila gene piwi.
657 *Blood* 97, 426–434.

658 Sierra, A., Martín-Suárez, S., Valcárcel-Martín, R., Pascual-Brazo, J., Aelvoet, S.-A., Abiega, O., Deudero,
659 J.J., Brewster, A.L., Bernales, I., Anderson, A.E., et al. (2015). Neuronal Hyperactivity Accelerates
660 Depletion of Neural Stem Cells and Impairs Hippocampal Neurogenesis. *Cell Stem Cell* 16, 488–503.

661 Toda, T., Parylak, S.L., Linker, S.B., and Gage, F.H. (2019). The role of adult hippocampal neurogenesis in
662 brain health and disease. *Mol. Psychiatry* 24, 67–87.

663 Torres, A.G., Reina, O., Attolini, C.S.O., and Ribas De Pouplana, L. (2019). Differential expression of
664 human tRNA genes drives the abundance of tRNA-derived fragments. *Proc. Natl. Acad. Sci. U. S. A.* 116,
665 8451–8456.

666 Vicidomini, G., Bianchini, P., and Diaspro, A. (2018). STED super-resolved microscopy. *Nat. Methods* 15,
667 173–182.

668 Viero, G., Lunelli, L., Passerini, A., Bianchini, P., Gilbert, R.J., Bernabò, P., Tebaldi, T., Diaspro, A.,
669 Pederzoli, C., and Quattrone, A. (2015). Three distinct ribosome assemblies modulated by translation are the
670 building blocks of polysomes. *J. Cell Biol.* 208, 581–596.

671 Wakisaka, K.T. (2019). The dawn of pirna research in various neuronal disorders. *Front. Biosci.* 24, 1440–
672 1451.

673 Walker, T.L., and Kempermann, G. (2014). One mouse, two cultures: Isolation and culture of adult neural
674 stem cells from the two neurogenic zones of individual mice. *J. Vis. Exp.* 1-9.

675 Walker, T.L., Overall, R.W., Vogler, S., Sykes, A.M., Ruhwald, S., Lasse, D., Ichwan, M., Fabel, K., and
676 Kempermann, G. (2016). Lysophosphatidic Acid Receptor Is a Functional Marker of Adult Hippocampal
677 Precursor Cells. *Stem Cell Reports* 6, 552–565.

678 Waterston, R.H., Lindblad-Toh, K., Birney, E., Rogers, J., Abril, J.F., Agarwal, P., Agarwala, R., Ainscough,
679 R., Alexandersson, M., An, P., et al. (2002). Initial sequencing and comparative analysis of the mouse
680 genome. *Nature* 420, 520–562.

681 Yu, C.-W. (1992). The assessment of cellular proliferation by immunohistochemistry: a review of currently
682 available methods and their applications.

683 Zhang, P., Si, X., Skogerbø, G., Wang, J., Cui, D., Li, Y., Sun, X., Liu, L., Sun, B., Chen, R., et al. (2014).
684 PiRBase: A Web resource assisting piRNA functional study. *Database* 2014, 1–7.

685 Zhao, P., Yao, M., Chang, S., Gou, L., Liu, M., and Qiu, Z. (2015). Novel function of PIWIL1 in neuronal
686 polarization and migration via regulation of microtubule-associated proteins. *Mol. Brain* 1–12.

687

688 **Acknowledgments**

689 We are grateful to G. Hannon (Cambridge, UK) for providing Mili, Miwi antibodies; G. Enikolopov (Stony
690 Brook Univ. NY, USA) for the Nestin-GFP mouse. We thank IIT technical staff (S. Bianchi; M. Pesce; E.
691 Albanesi, M. Morini, D. Vozzi) for excellent assistance and L. Pandolfini (IIT-CHT Genoa, Italy) for advice
692 in piRNA resistance to periodate oxidation and alkaline β -elimination protocol. **Funding:** This study was
693 supported by Fondazione Istituto Italiano di Tecnologia; by Fondazione Cariplo Grant #2015-0590 and
694 AIRC-IG 2017 # 20106 to DDPT. P.B. (UvA) and C.P.F. were funded by an ERA-NET-NEURON EJTC
695 2016 grant and by The Netherlands Organization for Scientific research (NWO). We apologize to those
696 colleagues whose work could not be cited due to space limitations.

697

698 **Author contributions**

699 Conceptualization: C.G., D.D.P.T.; Methodology and experiments: C.G, K.T., R.P., D.M., P.B. (UVA),
700 C.P.F., P.B. (IIT), M.S., M.P.E.; *In silico* analysis: A.L.V, R.M.C., G.P., K.T.; Data Curation and
701 visualization: C.G.; Writing – original draft preparation: C.G., D.D.P.T.; –Editing: all the authors;
702 Supervision: R.S., A.D., C.P.F., P.C., S.G.; D.D.P.T.; Project administration: D.D.P.T.; Funding acquisition:
703 D.D.P.T.

704

705 **Declaration of interests**

706 The authors declare no competing interests.

707

708 **Figure legends**

709 **Fig. 1. Hippocampal expression of Mili is enriched in aNPCs and decreases during neurogenesis.**

710 (A) Levels of PIWIL1 (Miwi), PIWIL2 (Mili) and PIWIL3 (Miwi2) transcripts in RNA seq. data from aNPCs
711 cultures in proliferative (Days of differentiation –DIF– 0) and differentiation media (DIF 4 to 14). (B) Mili
712 protein abundance in undifferentiated aNPCs (DIF0) and upon viral-induced neurogenesis (DIF4-14). (C)
713 Miwi and (D) Mili protein abundance in extracts from postnatal mouse testis, hippocampus and from
714 undifferentiated aNPCs cultures. (E) Mili protein abundance in in extracts from cultured mouse hippocampal
715 neurons and undifferentiated aNPCs. (F) Mili (white) expression in Td+ NSC (red) in hippocampal subgranular
716 zone (SGZ); arrows indicate Td+ Mili + double-positive cells. (G) Scheme of the experiment (top), *Mili* mRNA
717 expression in sorted Td+ and Td– cells after *in vivo* transduction with split-Cre viruses in the hippocampus
718 (bottom). Data are expressed as mean \pm SEM, n = 3 independent experiments. t-Student test or one-way
719 ANOVA Bonferroni as post hoc: *p < 0.05, **p < 0.01, **** p < 0.0001. GCL, granular cell layer; H, Hilus.
720 Scale bars: 10 μ m.

721

722 **Fig. 2. Level of piRNAs parallels Mili abundance in neurogenesis.**

723 (A) Size distribution of piRNA reads. (B) Uridine bias at piRNA 5' ends. (C) Probability of distances from
724 the 5'ends of putative secondary piRNAs to the 5'ends of putative primary piRNAs. Note that 5' termini of
725 putative primary and secondary piRNAs derived from the same cluster tend to concatenate around the '0'
726 mark, as reported in other animals. Distance probability was assayed for unique piRNAs (length between 15-
727 35 nucleotides), without taking into account abundance, by locally weighted smoothing linear regression
728 (LOWESS). (D) RNA relative expression of four of the top abundant piRNAs (in H) and two control
729 snoRNAs (202 and 135) in aNPC, upon treatment with sodium periodate (NaIO₄) or water and alkaline β -
730 elimination. Synthetic RNA oligos were used as negative (Unmethylated, UnMet) and positive (2'-O-
731 methylated, 2'OMet) controls, respectively. Note that presence of 3'-end 2'-O-methylation in positive
732 control and piRNAs confers them resistance to periodate oxidation and alkaline β -elimination, in contrast to
733 their depletion in UnMet negative control and snoRNAs. (E) *Mili* mRNA (left) and protein (right) levels in
734 aNPCs upon viral transduction of scrambled shRNA (Control) or shRNA targeting *Mili* (Mili KD). (F)
735 Expression of four of the most abundant piRNA clusters in control and Mili KD aNPCs. (G) Genomic

location of 298 piRNA clusters on mm9. (H) Mean reads of piRNA clusters in aNPCs (DIF0) and upon viral-induced neurogenesis (DIF4-7), where the total number of filtered reads in each library ranges between 1,4 - 4,4 x 10⁶. (I) (left) Schematic representation of the experiment; (right) expression of four of the most abundant piRNA clusters in sorted Td+ and Td- cells 10 dpi of split-Cre viruses in hippocampus. (L) Expression of piRNA clusters (left) and piR-cluster 1 (right) in human NSC and astrocytes. Data are expressed as mean ± SEM, n = 2 (A-C, G-H) and n = 3 (D-F, I) independent experiments. t-Student test as post hoc: *p < 0.05, **p < 0.01, *** p < 0.001, **** p < 0.0001.

Fig. 3. The piRNA pathway sustains proper neurogenesis.

(A) Scheme of the *in vivo* experiment. (B) *Mili* mRNA (left), protein (middle) and *Gfap* mRNA (right) levels in the hippocampus 48 hours after the injection of scrambled (Control) or GapmeR against *Mili* (*Mili* KD). (C) Light-microscopy images of postnatal hippocampal sections, immunostained for GFAP, 30 dpi of scrambled (Control, left hemisphere) and GapmeR against *Mili* (*Mili* KD, right hemisphere). (D) (Left) Immunostaining for GFAP (green), BrdU (red), NeuN (white) and nuclear DNA (blue) in the hippocampus 30 dpi of scrambled (Control) or GapmeR against *Mili* (*Mili* KD); (right) percentages of NeuN+BrdU+ (white arrowheads), or GFAP+BrdU+ (yellow arrowheads) over total BrdU+ cells. (E) mRNA expression of reactive astrocyte markers in the hippocampus 48h upon injection of scrambled (control) or GapmeR against *Mili* (*Mili* KD). (F) *Mili* mRNA (left) and piR-cluster 1 (right) expression in sorted GFP+ NSCs from Nestin-GFP mice treated with Saline (Control) or Kainic Acid (KA). Data are expressed as mean ± SEM, n = 3 independent experiments (A-C); n=5 (E); n = 7 (F, G); n = 3 (H, I). t-Student test as post hoc: *p < 0.05, **p < 0.01, **** p < 0.0001. Scale bars: 1 mm (C); 100 μm (D).

Fig. 4. Inhibition of the piRNA pathway in aNPCs induces senescence-associated phenotypes

(A) Heatmap showing the mRNA expression of genes involved in immune-modulatory and senescence associated genes in differentiating aNPCs at DIF4 upon *Mili* KD compared to control cells. Expression level represented in Transcript per Million (TPM). (B) Bright field microscopy images (left) and quantification (right) of β-galactosidase positive cells as percent of total cells upon *Mili* KD or control, 48 h after induction of spontaneous differentiation. (C) Fluorescence microscopy images (left) and quantification (right) of control

764 or Mili KD aNPCs 48h after spontaneous differentiation, immunostained with anti-BrdU (white) and Ki67
765 (purple) antibodies. (Right) Percentage of BrdU+ and Ki67- cells over BrdU+ cells. (D) (Top) Representative
766 cell cycle analysis of propidium iodide staining by flow cytometry; (Bottom) Percentage of aNPCs in G0/G1,
767 S and G2/M phases 48h after spontaneous differentiation. (E, F) Relative abundance of cell cycle-dependent
768 genes (E) and involved in cell cycle (F) in Control and Mili KD aNPCs 48 hours (E) or DIF4 (F) after
769 spontaneous differentiation. (G) (left) Scheme of the *in vivo* experiment; (right) *Mili* mRNA expression in
770 Nestin+ sorted cells from young (6 weeks) and old (56 weeks) mice. Data are expressed as mean \pm SEM, n =
771 3 independent, (in A, 2 separate flow cells per sample). t-Student test as post hoc: *p < 0.05, **p < 0.01,
772 ***p < 0.001, ****p < 0.0001. Scale bar, 50 μ m.

773

774 **Fig 5. piRNAs target noncoding RNAs and mRNAs involved in ribosome assembly and translation.**

775 (A, B) Pie plots showing proportions of noncoding RNAs predicted targets of piRNAs in undifferentiated
776 aNPCs (A, DIF0) and upon induction of neurogenesis (B, DIF4-7). (C) Transcription levels of SINE B1 and
777 5S rRNA, and (D) transcription levels of LINE1 5'UTR in the Mili KD aNSCs (DIF0) and differentiating
778 aNPC (DIF4-7). (E) Total counts of upregulated (black bars) and downregulated genes (white bars), for all
779 genes, all piRNA targeted genes and those with piRNA homology (indicated). (F) Scatter plot of all detected
780 genes in control or Mili KD aNPCs (black circles), piRNA target (red circles) and those with piRNA homology
781 (blue dots). (G) The log2 fold-change of significantly altered genic mRNA transcripts (abscissa) plotted with
782 the raw number of unique piRNA sequences qualified as targeting molecules (ordinate) for all modulated genes
783 (black circles), and piRNA-targeted genes (red dots), identified by RNA-Seq. The modulated genes without
784 targeting piRNAs concatenate at the bottom at the 'y = 0' value. Total range, inset. (H) The log2 fold-change
785 of significantly altered piRNA-targeted gene mRNA transcripts (abscissa) plotted with the summed levels of
786 all mRNA-targeting (complementary) piRNA molecules (ordinate), identified by RNA-Seq. (I) Bar graph
787 showing the top biological pathways significantly upregulated upon Mili KD; Numbers in each category
788 indicate gene counts. Data are expressed as mean \pm SEM, n = 3 independent experiments. t-Student test as
789 post hoc: *p < 0.05, **p < 0.01 (C & D). Significant difference was detected by the one-way ANOVA, p < 0.05
790 (G & H). Data are expressed in transcripts per million (TPM) as the mean levels of 6 sequencing runs for 3

791 samples. (E-I) transcriptome profiling at DIF4. Outliers (mean calculation) were detected by more than three
792 mean absolute deviations, for a final 'n' value between 4 and 6 samples.

793

794 **Fig. 6. Inhibition of the piRNA pathway in aNPCs enhances polysome assembly and results in higher**
795 **protein synthesis upon differentiation.**

796 (A, B) Microscopy images (Middle cut: g-STED nanoscopy; Bottom: Confocal; Top: analysis) of control and
797 Mili KD aNPCs (DIF 0 and 7) immunostained for the ribosomal protein RPL26. (Right) normalized
798 distributions of the occupancy, concentration and average of particle size of each polyribosome particle in the
799 indicated cells. (C) Protein synthesis rate (right) as determined by OPP incorporation assay with flow
800 cytometry (left) in control and Mili KD undifferentiated (DIF0) and differentiating (DIF 7) aNPCs. Scale bars:
801 2 (A); 10 (B) μm . Data are expressed as mean \pm SEM, n = 3 independent experiments. t-Student test as post
802 hoc: *p < 0.05.

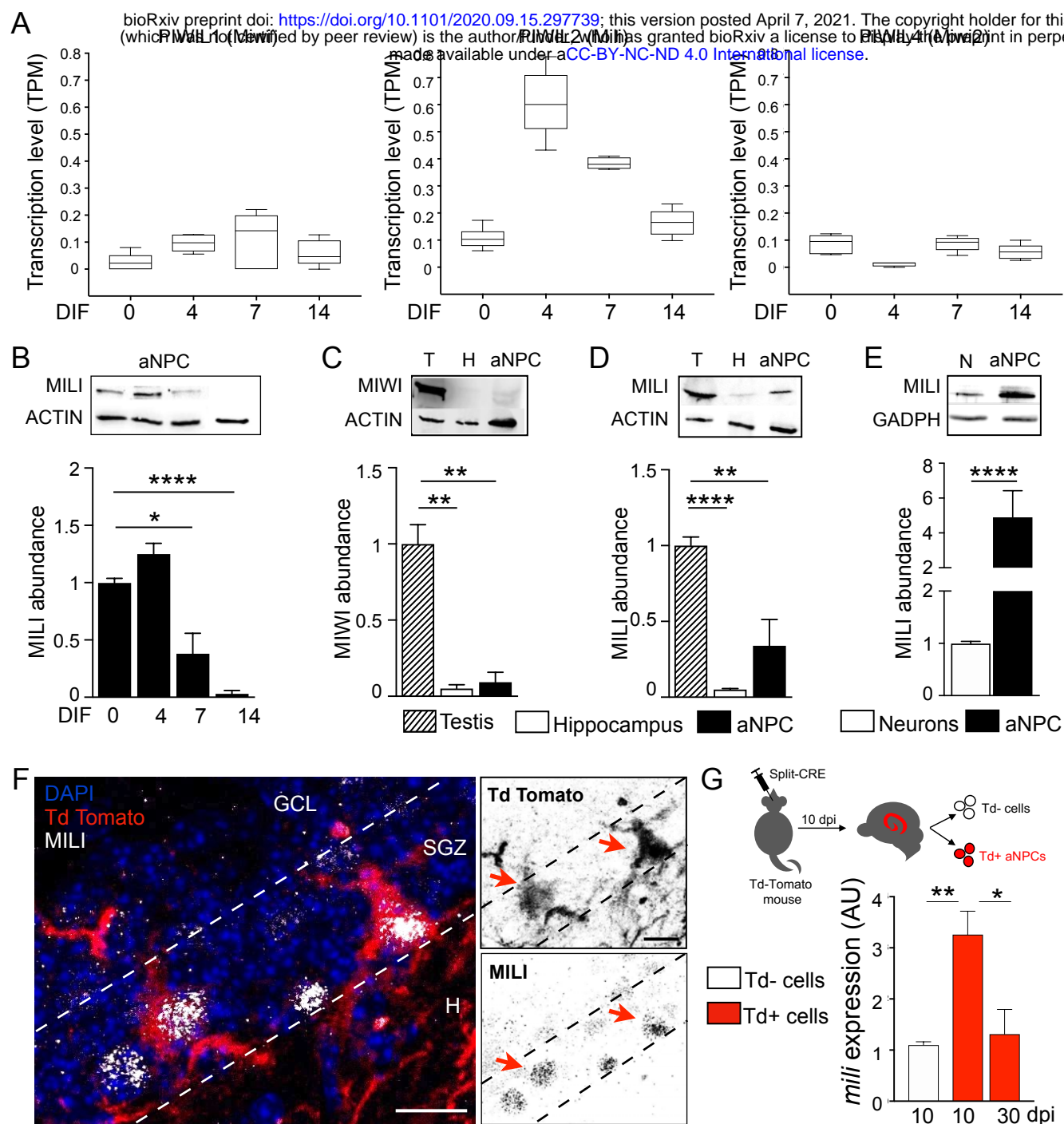


Fig. 1

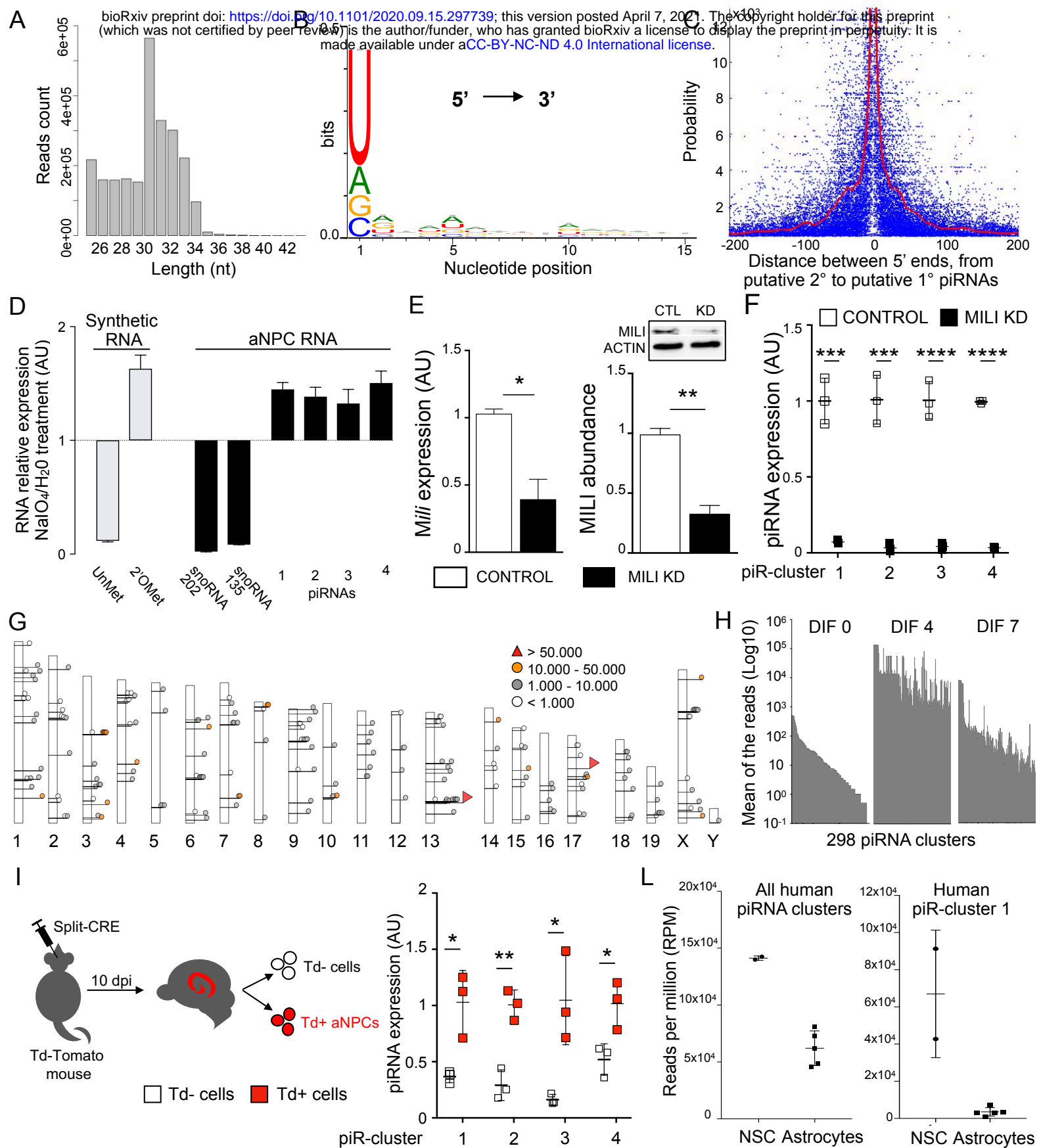


Fig. 2

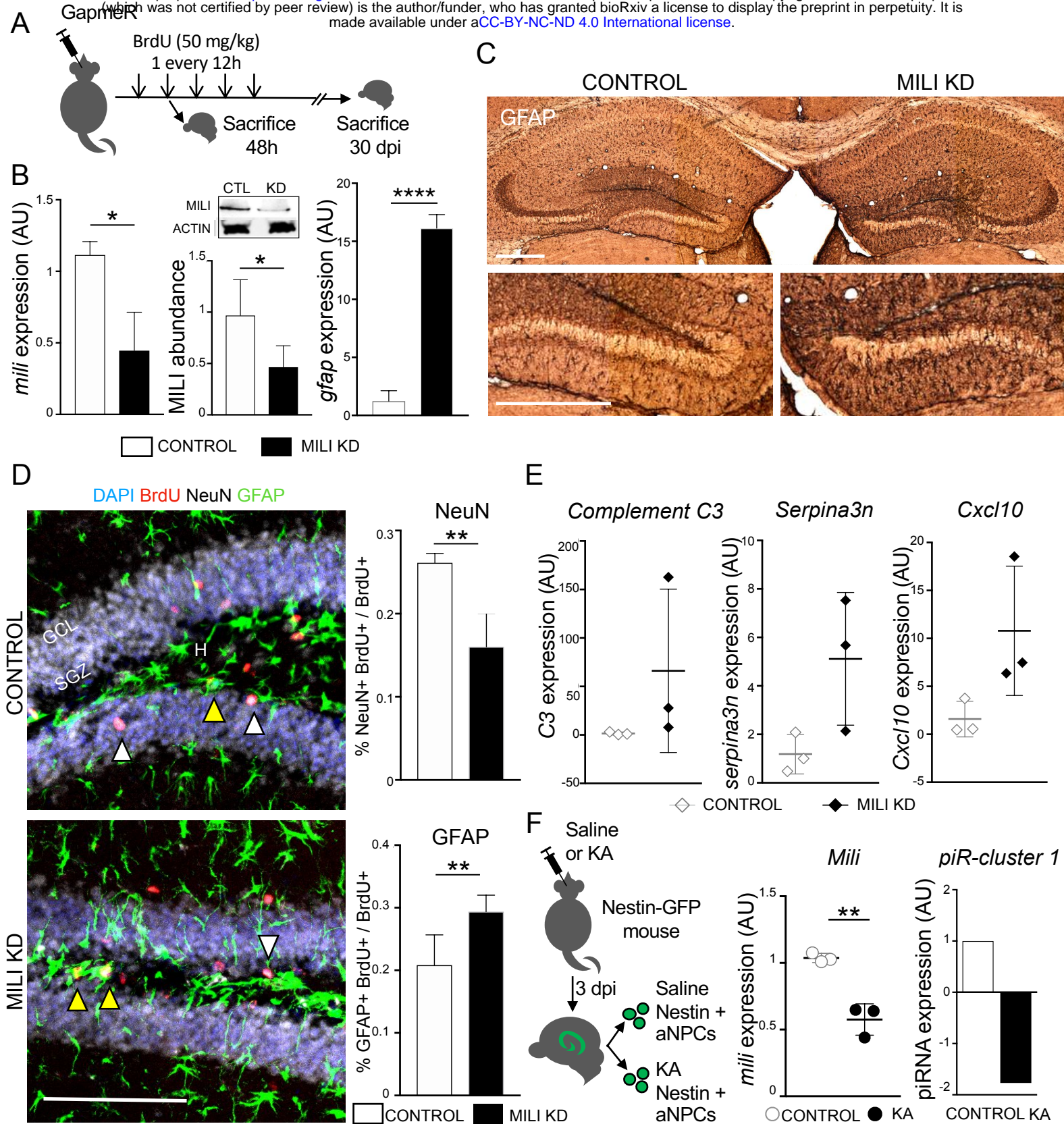


Fig. 3

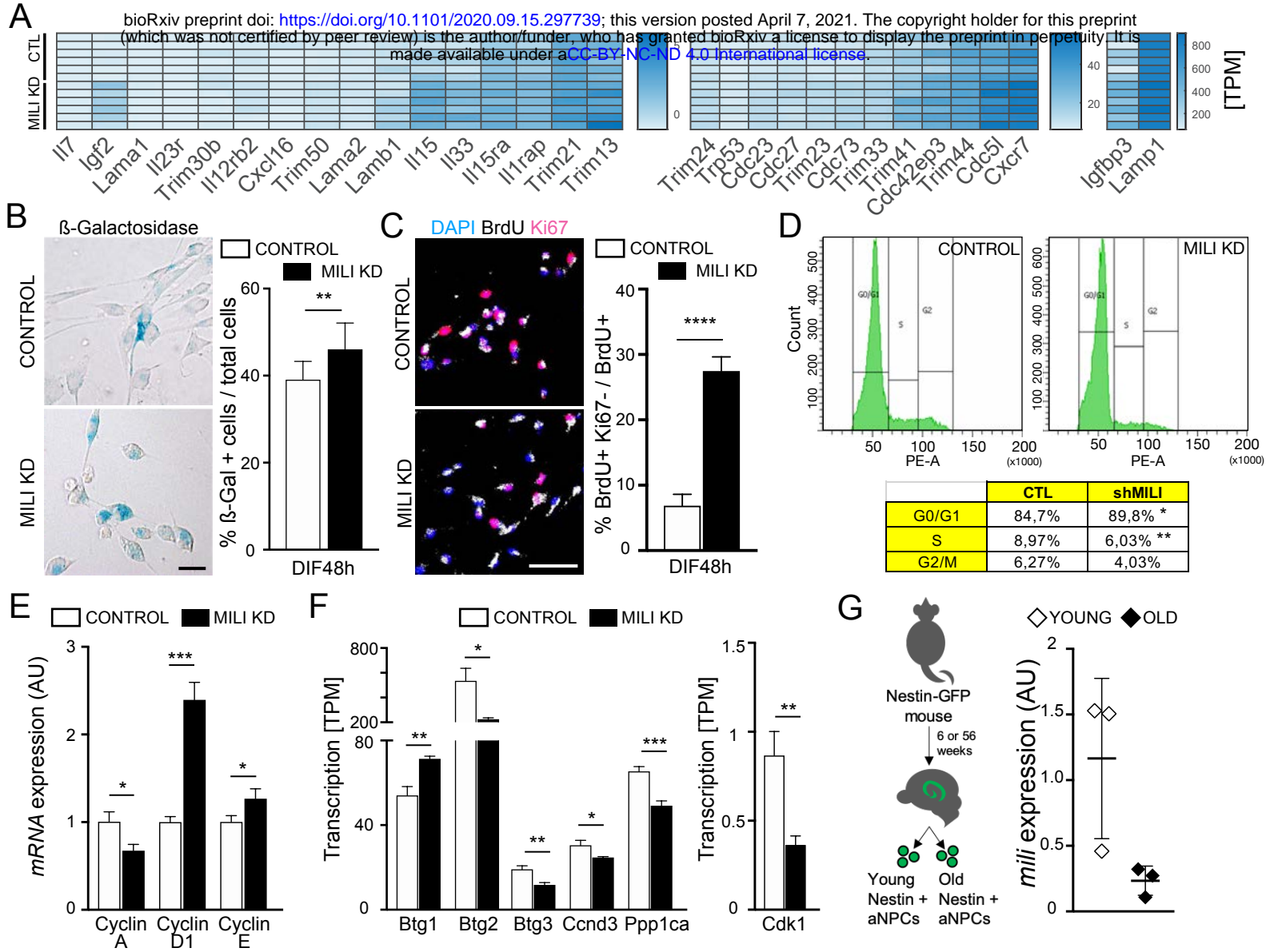


Fig. 4

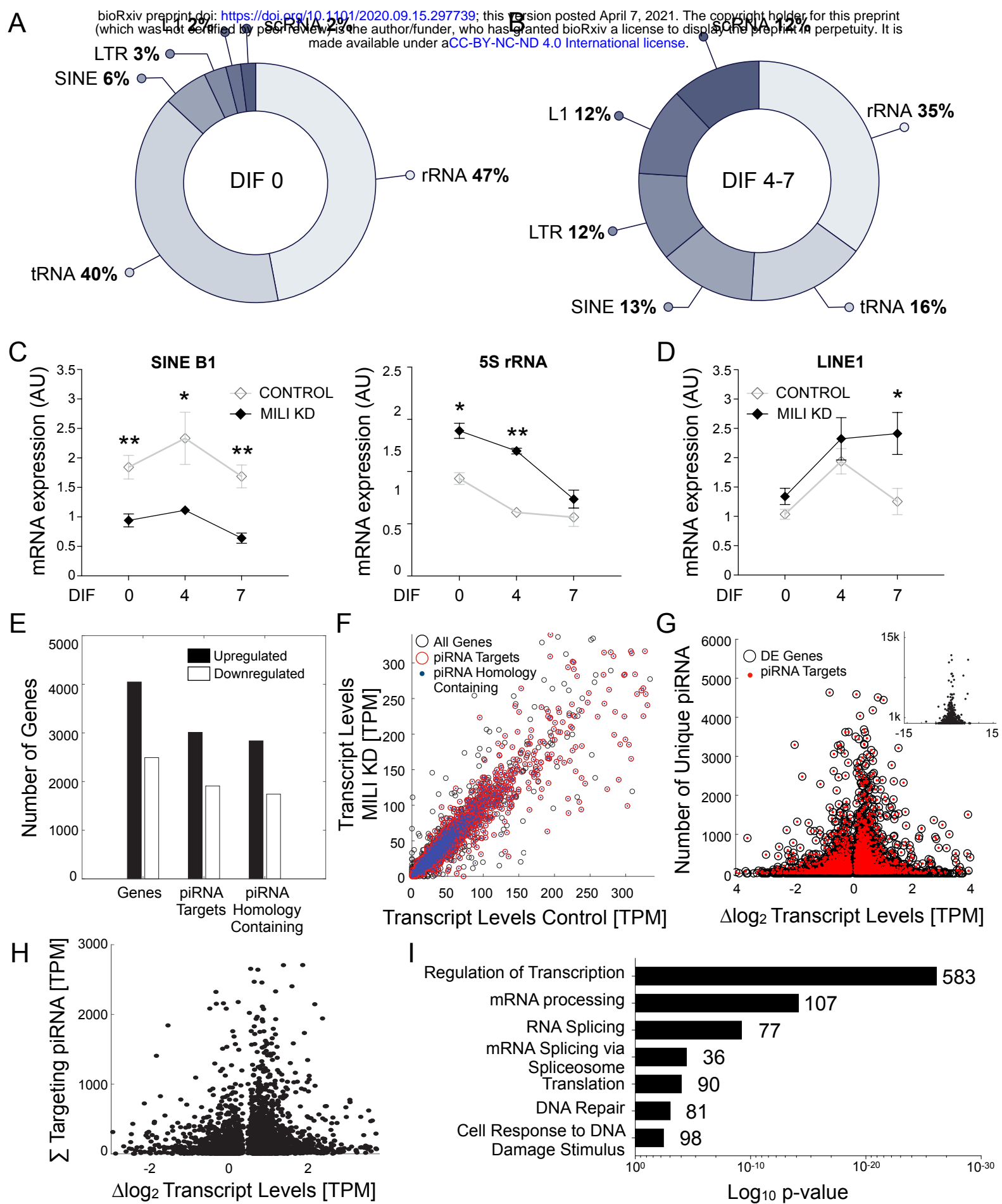


Fig.5

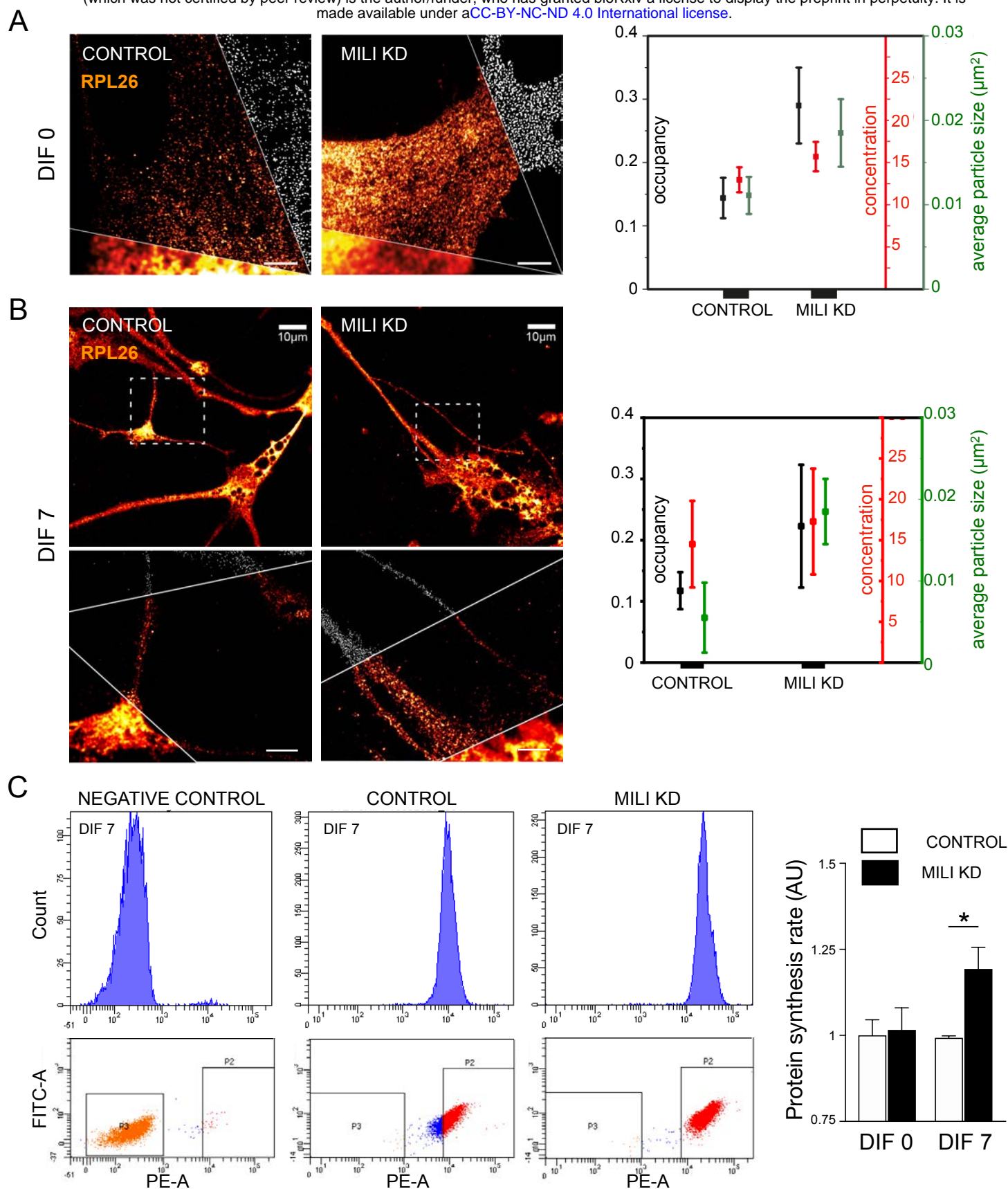


Fig. 6